The International Journal of Robotics Research
32(4) 446–457

DOI: 10.1177/0278364913482015
ijr.sagepub.com

Dynamic contact force/torque observer: Sensor fusion for improved interaction control

Georg Bätz[1], Bernhard Weber[1], Michael Scheint[1], Dirk Wollherr[1,2] and Martin Buss[1]

Abstract

The potential areas of application for robots have gradually extended beyond the classical industrial settings in large-scale enterprizes: nowadays, the integration of robots into daily life has become a central development in robotics. Here, one major challenge is the physical interaction with unknown and/or changing environments. Such an interaction requires knowledge of the exchanged contact forces and torques. To this end, robotic systems are typically equipped with force/torque sensors at the wrist. By using force control schemes that rely on measurements from these sensors, conventional manipulation tasks are successfully executed. In particular, for dynamic manipulation tasks, however, the problem arises that the inertial forces/torques of the end effector have a non-negligible effect on the measurements of the wrist sensor. This degrades the performance of the interaction control and constitutes a safety risk since the actual interaction forces/torques deviate from the desired values. As a solution to this problem, the paper discusses four contact force/torque observer designs: two approaches are based on the extended Kalman filter (EKF) and two approaches are based on the unscented Kalman filter (UKF). For both types, EKF and UKF, two different measurement vectors are considered: the first one only uses pose and force/torque measurements, whereas the second one also uses acceleration measurements to determine the contact forces and torques. The four observer designs are evaluated in simulation and experiment for six-degree-of-freedom (DOF) tasks.

Keywords

sensor fusion, interaction control, observer design

1. Introduction

The knowledge of contact forces and torques is particularly crucial for robots that physically interact with the environment (Khatib, 1987; Lefebvre, 2005; Siciliano et al., 2008). For dynamic manipulation tasks (Mason and Lynch, 1993), determining these contact forces/torques is a challenging task: Figure 1 illustrates the typical hardware setup with a force/torque (F/T) sensor located at the wrist. In general, the measured forces $\boldsymbol{F}_S$ and torques $\boldsymbol{M}_S$ are constituted by the following components

$$\begin{bmatrix} \boldsymbol{F}_S \\ \boldsymbol{M}_S \end{bmatrix} = \begin{bmatrix} \boldsymbol{F}_E \\ \boldsymbol{M}_E \end{bmatrix} + \begin{bmatrix} \boldsymbol{F}_I \\ \boldsymbol{M}_I \end{bmatrix} + \begin{bmatrix} \boldsymbol{F}_G \\ \boldsymbol{M}_G \end{bmatrix}, \quad (1)$$

where $\boldsymbol{F}_E, \boldsymbol{M}_E$ are the environmental contact forces and torques, $\boldsymbol{F}_I, \boldsymbol{M}_I$ are the inertial forces and torques, and $\boldsymbol{F}_G, \boldsymbol{M}_G$ are the forces and torques due to gravity. During dynamic motions, the problem arises that inertial forces/torques of the end effector have a significant effect on the force and torque measurements. Hence, the measurements do not correspond to the actual environmental interaction forces/torques.

1.1. Related work

The problem of contact F/T estimation has been addressed by various researchers: Uchiyama and Kitagaki (1989) were the first to investigate dynamic force sensing for high-speed robot manipulation tasks. The developed observer could estimate both environment forces and torques and was based on the extended Kalman filter (EKF). The observer design, however, was restricted to pose and F/T measurements only. In the presented results, the complexity of the problem was reduced by considering only a planar scenario with two translational and one rotational degree of freedom (DOF).

[1]Institute of Automatic Control Engineering, Technische Universität München, Munich, Germany
[2]Institute of Advanced Study, Technische Universität München, Munich, Germany

Corresponding author:
Georg Bätz, Institute of Automatic Control Engineering, Technische Universität München, Theresienstraße 90, D-80290 München, Germany.
Email: georg.baetz@tum.de

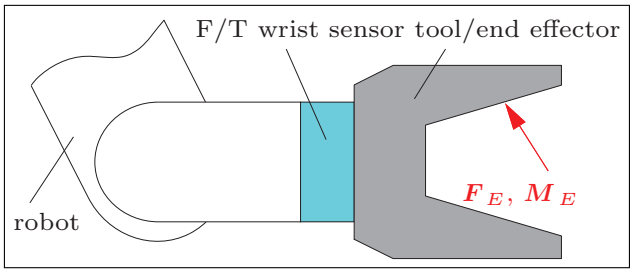

Fig. 1. Schematic of the hardware setup: the tool/end effector that interacts with the environment is attached to a wrist-mounted F/T sensor.

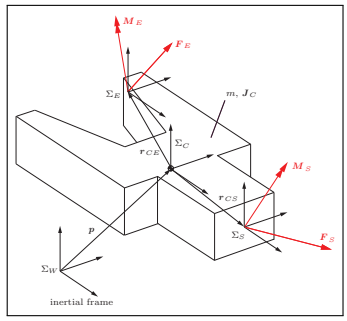

Fig. 2. Forces and moments applied at the end effector.

Lin (1997) developed an observer based on position and force measurements. In this work, only environment forces and translational motions were considered which results in linear process and measurement equations. Hence, a classical Kalman filter could be applied to estimate the contact forces.

Garcia et al. investigated a sensor fusion approach for dynamic F/T estimation (Garcia et al., 2004, 2005b,a, 2006, 2008). In addition to pose and F/T measurements, an inertial sensor was used to measure the tool acceleration. In the EKF-based observer design, the environment forces and torques were not considered. The estimation error was utilized to obtain a contact F/T estimator with low-pass properties. Considering the nonlinear process model for the torques, it seems problematic to use the estimation error of such an observer to determine the environment torques. In addition, the representation of the tool orientation with Euler angles appears critical because of the well-known issues with representation singularities.

Kröger et al. (2006) also discussed a fusion of F/T and acceleration information for contact F/T estimation. In their work, characteristic properties of F/T and acceleration sensors were reported (Kubus et al., 2008). Furthermore, translational and rotational acceleration estimates based on pose measurements were derived. However, the calculation of contact forces and torques was performed without considering the stochastic properties of the signals, hence limiting the effectiveness of the approach. For a contour following task, Koch et al. (2011) compensated for inertial forces of the tool in contact F/T measurements using acceleration sensors. Again, stochastic properties of the acceleration signals were neglected.

1.2. Contribution

The paper evaluates four observer designs that reconstruct the contact forces/torques during dynamic motions and are thus crucial to improve the performance of robot interaction control schemes. To this end, the paper first presents the continuous and discrete-time model for the system (Section 2). The orientation of the tool is described with quaternion notation. Then, the design of a six-DOF F/T observer is detailed: in addition to an EKF-based design, the paper also discusses an observer based on the unscented Kalman filter (UKF). For both filter types, two different measurement vectors are considered: one using only pose and F/T measurements and one using additional acceleration and velocity measurements (Section 3). The performance of the resulting four different filter designs is evaluated for six-DOF tasks in simulation and experiment (Sections 4 and 5). The evaluation also considers the robustness of the filter towards changing operating conditions, since this aspect is of particular importance for hardware applications.

2. System model

Let C denote the center of mass of the end effector and Σ_C the body-fixed coordinate frame with origin in C and which axes coincide with the principal axes of inertia of the end effector. Similarly, as shown in Figure 2 the world frame is denoted by Σ_W, the frame of the end effector contact point by Σ_E, and the F/T sensor frame as Σ_S. Using the center of mass C as the reference point, the Newton–Euler equations for the end effector with respect to frame Σ_C (illustrated by the superscript C) are given by (Wittenburg, 2007)

$$\begin{aligned} \boldsymbol{F}_S^C - \boldsymbol{F}_E^C + m\boldsymbol{g}^C &= m\boldsymbol{a}_C^C \\ \boldsymbol{S}(\boldsymbol{r}_{CS}^C)\boldsymbol{F}_S^C + \boldsymbol{M}_S^C - \boldsymbol{S}(\boldsymbol{r}_{CE}^C)\boldsymbol{F}_E^C - \boldsymbol{M}_E^C &= \boldsymbol{J}_C^C\boldsymbol{\alpha}^C + \boldsymbol{S}\left(\boldsymbol{\omega}^C\right)\boldsymbol{J}_C^C\boldsymbol{\omega}^C. \end{aligned} \tag{2}$$

Here, the tool mass is given by m, $\boldsymbol{J}_C^C$ is the moment of inertia with respect to C, $\boldsymbol{a}_C^C$ denotes the translational end effector acceleration, $\boldsymbol{\omega}^C/\boldsymbol{\alpha}^C$ the angular end effector velocity/acceleration, and $\boldsymbol{g}^C$ the vector of gravitational acceleration. Here $\boldsymbol{S}(\boldsymbol{b}) = \boldsymbol{S}_{\boldsymbol{b}}$ is the skew-symmetry operator applied to vector $\boldsymbol{b}$. The matrix $\boldsymbol{R}_j^i$ is the rotation matrix of frame Σ_j with respect to frame Σ_i.

It should be noted that most quantities in (2) are measured (calculated) in their own frame. Thus, an extended formulation of the Newton–Euler equations for the actual implementation is

$$\begin{aligned} \boldsymbol{R}_S^C\boldsymbol{F}_S^S - \boldsymbol{R}_E^C\boldsymbol{F}_E^E + m\boldsymbol{R}_W^C\boldsymbol{g}^W &= m\boldsymbol{R}_I^C\boldsymbol{a}_C^I \\ \boldsymbol{S}\left(\boldsymbol{r}_{CS}^C\right)\boldsymbol{R}_S^C\boldsymbol{F}_S^S + \boldsymbol{R}_S^C\boldsymbol{M}_S^S - \boldsymbol{S}\left(\boldsymbol{r}_{CE}^C\right)\boldsymbol{R}_E^C\boldsymbol{F}_E^E & \\ -\boldsymbol{R}_E^C\boldsymbol{M}_E^E = \boldsymbol{J}_C^C\boldsymbol{R}_I^C\boldsymbol{\alpha}^I + \boldsymbol{S}\left(\boldsymbol{R}_I^C\boldsymbol{\omega}^I\right)\boldsymbol{J}_C^C\boldsymbol{R}_I^C\boldsymbol{\omega}^I. & \end{aligned} \tag{3}$$

In matrix notation, one obtains the relation

$$\begin{bmatrix} \boldsymbol{F}^C_{S\to C} \\ \boldsymbol{M}^C_{S\to C} \end{bmatrix} - \begin{bmatrix} \boldsymbol{F}^C_{E\to C} \\ \boldsymbol{M}^C_{E\to C} \end{bmatrix} = \begin{bmatrix} m\,\boldsymbol{R}^C_I & \boldsymbol{0} \\ \boldsymbol{0} & \boldsymbol{J}^C_C\,\boldsymbol{R}^C_I \end{bmatrix} \begin{bmatrix} \boldsymbol{a}^I_C \\ \boldsymbol{\alpha}^I \end{bmatrix} + \begin{bmatrix} -m\boldsymbol{R}^C_W & \boldsymbol{0} \\ \boldsymbol{0} & \boldsymbol{S}\left(\boldsymbol{R}^C_I\boldsymbol{\omega}^I\right)\boldsymbol{J}^C_C\boldsymbol{R}^C_I \end{bmatrix} \begin{bmatrix} \boldsymbol{g}^W \\ \boldsymbol{\omega}^I \end{bmatrix}, \tag{4}$$

where the expressions $\boldsymbol{F}^C_{j\to C}$, $\boldsymbol{M}^C_{j\to C}$ with $j \in \{S, E\}$ correspond to

$$\begin{bmatrix} \boldsymbol{F}^C_{j\to C} \\ \boldsymbol{M}^C_{j\to C} \end{bmatrix} = \begin{bmatrix} \boldsymbol{R}^C_j & \boldsymbol{0} \\ \boldsymbol{S}\left(\boldsymbol{r}^C_{Cj}\right)\boldsymbol{R}^C_j & \boldsymbol{R}^C_j \end{bmatrix} \begin{bmatrix} \boldsymbol{F}^j_j \\ \boldsymbol{M}^j_j \end{bmatrix}. \tag{5}$$

2.1. Continuous-time system model

In the following, all quantities are expressed in frame Σ_C and in order to facilitate the notation, the superscript C is omitted. However, velocities and acceleration are absolute quantities calculated with respect to the inertial frame (and only expressed in frame C). Let $\boldsymbol{x} \in \mathbb{R}^{25}$ with

$$\boldsymbol{x} = \begin{bmatrix} \boldsymbol{p}^{\mathrm{T}} & \boldsymbol{o}^{\mathrm{T}} & \boldsymbol{v}^{\mathrm{T}} & \boldsymbol{\omega}^{\mathrm{T}} & \boldsymbol{F}^{\mathrm{T}}_S & \boldsymbol{F}^{\mathrm{T}}_E & \boldsymbol{M}^{\mathrm{T}}_S & \boldsymbol{M}^{\mathrm{T}}_E \end{bmatrix}^{\mathrm{T}} \tag{6}$$

denote the state vector of the system. Here, $\boldsymbol{p} \in \mathbb{R}^3$ and $\boldsymbol{o} \in \mathbb{R}^4$ are the position and orientation (in quaternion) of the tools center of mass with respect to the inertial frame and $\boldsymbol{v}$ is the (absolute) translational tool velocity. In the following, two different measurement vectors

$$\boldsymbol{y}_1 = \begin{bmatrix} \boldsymbol{p}^{\mathrm{T}} & \boldsymbol{o}^{\mathrm{T}} & \boldsymbol{F}^{\mathrm{T}}_S & \boldsymbol{M}^{\mathrm{T}}_S \end{bmatrix}^{\mathrm{T}} \in \mathbb{R}^{13} \tag{7}$$
$$\boldsymbol{y}_2 = \begin{bmatrix} \boldsymbol{p}^{\mathrm{T}} & \boldsymbol{o}^{\mathrm{T}} & \boldsymbol{F}^{\mathrm{T}}_S & \boldsymbol{M}^{\mathrm{T}}_S & \boldsymbol{a}^{\mathrm{T}} & \boldsymbol{\alpha}^{\mathrm{T}} & \boldsymbol{\omega}^{\mathrm{T}} \end{bmatrix}^{\mathrm{T}} \in \mathbb{R}^{22}$$

will be considered. While $\boldsymbol{y}_1$ relies solely on position and F/T measurements, $\boldsymbol{y}_2$ also includes acceleration and (rotational) velocity measurements. Based on (4) the nonlinear, continuous-time system model

$$\begin{aligned} \dot{\boldsymbol{x}} &= \boldsymbol{f}_c(\boldsymbol{x}, \boldsymbol{w}) \\ \boldsymbol{y}_i &= \boldsymbol{h}_{c,i}(\boldsymbol{x}, \boldsymbol{v}), \quad i \in \{1, 2\} \end{aligned} \tag{8}$$

can be derived. Here, the variables $\boldsymbol{w}$ and $\boldsymbol{v}$ represent the process and measurement noise. They are assumed to be white, independent of each other, and with normal probability distributions

$$\begin{aligned} \boldsymbol{p}(\boldsymbol{w}) &\sim \mathcal{N}(\boldsymbol{0}, \boldsymbol{Q}) \\ \boldsymbol{p}(\boldsymbol{v}) &\sim \mathcal{N}(\boldsymbol{0}, \boldsymbol{R}), \end{aligned} \tag{9}$$

where the process and measurement noise covariances $\boldsymbol{Q}$, $\boldsymbol{R}$ can vary with each measurement or time step. As proposed by Uchiyama and Kitagaki (1989), we assume that the process model for the sensor and environment forces and torques can be approximated by a white and Gaussian process.

2.2. Discrete-time system model

The nonlinear process and measurement model are given by the stochastic difference equation

$$\begin{aligned} \boldsymbol{x}_{[k+1]} &= \boldsymbol{f}(\boldsymbol{x}_{[k]}, \boldsymbol{w}_{[k]}), \\ \boldsymbol{y}_{i,[k+1]} &= \boldsymbol{h}_i(\boldsymbol{x}_{[k+1]}, \boldsymbol{v}_{[k+1]}), \quad i \in \{1, 2\}, \end{aligned} \tag{10}$$

where the subscripts $[k+1], [k]$ denote the discrete time steps and $\boldsymbol{w}k$ and $\boldsymbol{v}_{[k]}$ represent the discrete process and measurement noise with covariance matrices $\boldsymbol{Q}_{[k]} = \boldsymbol{Q}(t_{[k]})$ and $\boldsymbol{R}_{[k]} = \boldsymbol{R}(t_{[k]})$. The detailed process equation is given by

$$\begin{bmatrix} \boldsymbol{p}_{[k+1]} \\ \boldsymbol{o}_{[k+1]} \\ \boldsymbol{v}_{[k+1]} \\ \boldsymbol{\omega}_{[k+1]} \\ \boldsymbol{F}_{S[k+1]} \\ \boldsymbol{F}_{E[k+1]} \\ \boldsymbol{M}_{S[k+1]} \\ \boldsymbol{M}_{E[k+1]} \end{bmatrix} = \begin{bmatrix} \boldsymbol{p}_{[k]} + T\boldsymbol{v}_{[k]} + 0.5\frac{T^2}{m}\left(\boldsymbol{F}_{S[k]} - \boldsymbol{F}_{E[k]} + m\boldsymbol{g}\right) + \boldsymbol{w}_{p,[k]} \\ \boldsymbol{o}_{[k]} * \boldsymbol{o}_w * \boldsymbol{o}_\Delta \\ \boldsymbol{v}_{[k]} + \frac{T}{m}\left(\boldsymbol{F}_{S[k]} - \boldsymbol{F}_{E[k]} + m\boldsymbol{g}\right) + \boldsymbol{w}_{v,[k]} \\ \boldsymbol{\omega}_{[k]} + T\boldsymbol{J}_C^{-1}\left(\boldsymbol{S}_{r_{CS}}\boldsymbol{F}_{S[k]} - \boldsymbol{S}_{r_{CE}}\boldsymbol{F}_{E[k]} + \boldsymbol{M}_{S[k]} - \boldsymbol{M}_{E[k]} - \boldsymbol{S}_{\omega_{[k]}}\boldsymbol{J}_C\boldsymbol{\omega}_{[k]}\right) + \boldsymbol{w}_{\omega,[k]} \\ \boldsymbol{F}_{S[k]} + \boldsymbol{w}_{F_S,[k]} \\ \boldsymbol{F}_{E[k]} + \boldsymbol{w}_{F_E,[k]} \\ \boldsymbol{M}_{S[k]} + \boldsymbol{w}_{M_S,[k]} \\ \boldsymbol{M}_{E[k]} + \boldsymbol{w}_{M_E,[k]} \end{bmatrix} \tag{11}$$

where $*$ represents the quaternion multiplication. Here, $\boldsymbol{o}_w = \boldsymbol{w}_{o,[k]}$ is the quaternion reflecting process noise and

$$\begin{aligned} \boldsymbol{o}_\Delta &= \{\eta_\Delta, \boldsymbol{\epsilon}_\Delta\} \\ &= \left\{\cos\left(\frac{1}{2}\left|\left|\boldsymbol{\omega}_{[k]}\right|\right| T\right), \frac{\boldsymbol{\omega}_{[k]}}{\left|\left|\boldsymbol{\omega}_{[k]}\right|\right|}\sin\left(\frac{1}{2}\left|\left|\boldsymbol{\omega}_{[k]}\right|\right| T\right)\right\} \end{aligned} \tag{12}$$

denotes the differential rotation during the time interval T (Kraft, 2003; Natale, 2003). As the measurement equations for $\boldsymbol{y}_1$ are linear, they can be written in the following matrix notation

$$\begin{aligned} \boldsymbol{y}_{1,[k+1]} &= \begin{bmatrix} \boldsymbol{I}_{7\times 7} & \boldsymbol{0}_{7\times 6} & \boldsymbol{0}_{7\times 6} & \boldsymbol{0}_{7\times 6} \\ \boldsymbol{0}_{6\times 7} & \boldsymbol{0}_{6\times 6} & \boldsymbol{I}_{6\times 6} & \boldsymbol{0}_{6\times 6} \end{bmatrix} \boldsymbol{x}_{[k+1]} + \boldsymbol{v}_{[k+1]} \\ &= \boldsymbol{H}_1\boldsymbol{x}_{[k+1]} + \boldsymbol{v}_{1,[k+1]}. \end{aligned} \tag{13}$$

Owing to the incorporation of the angular acceleration, the measurement equations for $\boldsymbol{y}_2$ are nonlinear:

$$\boldsymbol{y}_{2,[k+1]} = \begin{bmatrix} \boldsymbol{H}_1 \boldsymbol{x}_{[k+1]} + \boldsymbol{v}_{1,[k+1]} \\ \frac{1}{m}\left(\boldsymbol{F}_{S[k+1]} - \boldsymbol{F}_{E[k+1]} + m\boldsymbol{g}\right) + \boldsymbol{v}_{a,[k+1]} \\ \boldsymbol{J}_C^{-1}\left(\boldsymbol{S}_{\boldsymbol{r}_{CS}}\boldsymbol{F}_{S[k+1]} - \boldsymbol{S}_{\boldsymbol{r}_{CE}}\boldsymbol{F}_{E[k+1]} + \boldsymbol{M}_{S[k+1]} - \boldsymbol{M}_{E[k+1]} - \boldsymbol{S}_{\boldsymbol{\omega}_{[k+1]}}\boldsymbol{J}_C\boldsymbol{\omega}_{[k+1]}\right) + \boldsymbol{v}_{\alpha,[k+1]} \\ \boldsymbol{\omega}_{[k+1]} + \boldsymbol{v}_{\omega,[k+1]} \end{bmatrix}. \tag{14}$$

3. Filter design

As shown in (11), the system is characterized by a nonlinear process model. In addition, the measurement model for $\boldsymbol{y}_2$ is also nonlinear, cf. (14). Hence, a nonlinear filter design is needed for the six-DOF dynamic F/T observer. In the following, two different approaches for nonlinear systems will be evaluated: the EKF and the UKF. For both approaches, one filter design with $\boldsymbol{y}_1$ and one design with $\boldsymbol{y}_2$ will be considered.

3.1. Extended Kalman filter

The EKF extends the Kalman filter for nonlinear systems by linearizing about the current mean and covariance and can, hence, be applied to the given nonlinear estimation problem (Welch and Bishop, 2006). Notating the partial derivatives as

$$\begin{aligned} \boldsymbol{A}_{[k]} &= \frac{\partial \boldsymbol{f}(\hat{\boldsymbol{x}}_{[k-1]}, \boldsymbol{0})}{\partial \boldsymbol{x}}, & \boldsymbol{W}_{[k]} &= \frac{\partial \boldsymbol{f}(\hat{\boldsymbol{x}}_{[k-1]}, \boldsymbol{0})}{\partial \boldsymbol{w}} \\ \boldsymbol{H}_{i,[k]} &= \frac{\partial \boldsymbol{h}_i(\hat{\boldsymbol{x}}_{[k-1]}, \boldsymbol{0})}{\partial \boldsymbol{x}}, & \boldsymbol{V}_{i,[k]} &= \frac{\partial \boldsymbol{h}_i(\hat{\boldsymbol{x}}_{[k-1]}, \boldsymbol{0})}{\partial \boldsymbol{v}}, \end{aligned} \tag{15}$$

the EKF time update equations are given by

$$\begin{aligned} \hat{\boldsymbol{x}}_{[k]}^- &= \boldsymbol{f}(\hat{\boldsymbol{x}}_{[k-1]}^-, \boldsymbol{0}) \\ \boldsymbol{P}_{[k]}^- &= \boldsymbol{A}_{[k]}\boldsymbol{P}_{[k-1]}\boldsymbol{A}_{[k]}^{\mathrm{T}} + \boldsymbol{W}_{[k]}\boldsymbol{Q}_{[k-1]}\boldsymbol{W}_{[k]}^{\mathrm{T}}. \end{aligned} \tag{16}$$

The equations in (16) predict the state $\boldsymbol{x}_{[k]}$ and the error covariance $\boldsymbol{P}_{[k]}$ at time step k based on the results from the previous time step $k-1$.

Then, the EKF measurement update equations are used to correct these predictions based on the actual measurements at time step k:

$$\begin{aligned} \boldsymbol{K}_{[k]} &= \boldsymbol{P}_{[k]}^- \boldsymbol{H}_{i,[k]}^{\mathrm{T}} \left(\boldsymbol{H}_{i,[k]}\boldsymbol{P}_{[k]}^-\boldsymbol{H}_{i,[k]}^{\mathrm{T}} + \boldsymbol{V}_{i,[k]}\boldsymbol{R}_{[k]}\boldsymbol{V}_{i,[k]}^{\mathrm{T}}\right)^{-1} \\ \hat{\boldsymbol{x}}_{[k]} &= \hat{\boldsymbol{x}}_{[k]}^- + \boldsymbol{K}_{[k]}\left(\boldsymbol{y}_{i,[k]} - \boldsymbol{h}_i(\hat{\boldsymbol{x}}_{[k]}^-, \boldsymbol{0})\right) \\ \boldsymbol{P}_{[k]} &= (\boldsymbol{I}_{25\times 25} - \boldsymbol{K}_{[k]}\boldsymbol{H}_{i,[k]})\,\boldsymbol{P}_{[k]}^-. \end{aligned} \tag{17}$$

The first equation computes the Kalman gain $\boldsymbol{K}_{[k]}$, the second updates the estimate $\hat{\boldsymbol{x}}_{[k]}$ with the current measurement $\boldsymbol{y}_{i,[k]}$ and the third equation updates the error covariance $\boldsymbol{P}_{[k]}$.

3.2. Unscented Kalman filter

As detailed in the previous paragraph, the EKF approximates the state distribution by a Gaussian random variable, which is then propagated through the first-order linearization of the nonlinear system. This can introduce large errors in the mean and covariance, particularly if the system is highly nonlinear on the considered time scale.

The UKF is based on the intuition that, when having a fixed number of parameters, it is easier to approximate a Gaussian distribution than it is to approximate an arbitrary nonlinear function (Julier et al., 1995). Hence, instead of a linearization, the UKF uses a set of deterministic sample points (sigma points) to parameterize the mean and the covariance. The state distribution is still approximated by a Gaussian random variable, but is now represented through the set of sigma points. The sample points capture the true mean and covariance of the Gaussian random variable. The sigma points are then propagated through the actual nonlinear system (and not through a linearization).

In the following, the basic algorithm of the UKF is summarized: for the detailed idea and implementation notes of the filter, see Julier and Uhlmann (1997, 2004). For a state vector $\boldsymbol{x}$ of dimension L, the $2L+1$ sigma points (vectors) $\boldsymbol{\chi}_i$ and their corresponding weights for the covariance $\boldsymbol{G}_i^{(c)}$ and the mean $\boldsymbol{G}_i^{(m)}$ are created according to the following procedure

$$\begin{aligned} \boldsymbol{\chi}_0 &= \boldsymbol{x}_{[k]} \\ \boldsymbol{\chi}_i &= \begin{cases} \boldsymbol{x}_{[k]} + \left(\sqrt{(L+\lambda)\boldsymbol{P}_{[k]}}\right)_i & \text{for } i = 1,\ldots,L \\ \boldsymbol{x}_{[k]} - \left(\sqrt{(L+\lambda)\boldsymbol{P}_{[k]}}\right)_{i-L} & \text{for } i = L{+}1,\ldots,2L \end{cases} \\ \boldsymbol{G}_0^{(c)} &= \frac{\lambda}{L+\lambda} + \left(1 - \alpha^2 + \beta\right) \qquad \boldsymbol{G}_0^{(m)} = \frac{\lambda}{L+\lambda} \\ \boldsymbol{G}_i^{(c)} &= \boldsymbol{G}_i^{(m)} = \frac{1}{2\,(L+\lambda)} \qquad \text{for } i = 1,\ldots,2L \\ &\text{with } \lambda = \alpha^2(L+\kappa) - L \quad \text{and} \quad L = \dim(\boldsymbol{x})\,. \end{aligned} \tag{18}$$

Here, $\boldsymbol{P}_{[k]}$ is the covariance matrix of $\boldsymbol{x}_{[k]}$ and $\left(\sqrt{(L+\lambda)\boldsymbol{P}_{[k]}}\right)_i$ the ith column of the matrix square root. The parameters α and κ define the distribution of the sigma points around the mean and are typically set to small positive values. The parameter β is used to include prior knowledge on the distribution of $\boldsymbol{x}_{[k]}$. For Gaussian distributions, the optimal choice is $\beta = 2$ (Wan and Van Der Merwe, 2000). For the UKF-based observers in this work, the parameters are set to $\alpha = 10^{-3}$, $\kappa = 0$, and $\beta = 2$.

4. Simulation

The purpose of the following simulation study is the evaluation of the four observer designs (EKF with $\boldsymbol{y}_1$, EKF with $\boldsymbol{y}_2$, UKF with $\boldsymbol{y}_1$, UKF with $\boldsymbol{y}_2$). In particular, the simulation of the system facilitates the investigation of the observer performance for changing environment conditions. In the following, this will be denoted as scenario I.

While gravity has a significant effect on the measured forces and torques, the compensation is relatively easy as its influence is only configuration-dependent. In contrast, the compensation of inertial effects is more challenging since these forces/torques also depend on acceleration and (rotational) velocity. Hence, to facilitate the presentation and discussion of the results, zero gravity was assumed in the simulation.

4.1. Scenario

The sampling time of the filter is $T = 1$ ms. The tool mass is $m = 2$ kg and the inertia tensor $\boldsymbol{J}_C^C = \text{diag}([3, 2, 1])$ kg m^2. The vector from the center of gravity to the force sensor coordinate frame is $\boldsymbol{r}_{CS}^C = [0.1\text{ m}, 0.1\text{ m}, 0.1\text{ m}]^{\mathrm{T}}$. In the simulation, the contact point of the tool with the environment coincides with the center of gravity. The process noise covariance is set to

$$\begin{aligned} \boldsymbol{Q} &= \text{diag}\left(\left[\boldsymbol{Q}_p, \boldsymbol{Q}_o, \boldsymbol{Q}_{v,t}, \boldsymbol{Q}_{v,r}, \boldsymbol{Q}_{F_S}, \boldsymbol{Q}_{F_E}, \boldsymbol{Q}_{M_S}, \boldsymbol{Q}_{M_E}\right]\right) \\ \text{with } \boldsymbol{Q}_p &= 0.5T^4/m^2\boldsymbol{I}_{3\times3} \quad \boldsymbol{Q}_o = 0.5T^4\boldsymbol{J}_C^{-1}\boldsymbol{J}_C^{-1}\boldsymbol{I}_{3\times3} \\ \boldsymbol{Q}_{v,t} &= T^2/m^2\boldsymbol{I}_{3\times3} \quad \boldsymbol{Q}_{v,r} = T^2\boldsymbol{J}_C^{-1}\boldsymbol{J}_C^{-1}\boldsymbol{I}_{3\times3} \\ \boldsymbol{Q}_{F_S} &= \boldsymbol{Q}_{M_S} = \boldsymbol{Q}_{F_E} = \boldsymbol{Q}_{M_E} = 100T^2\boldsymbol{I}_{3\times3}. \end{aligned} \tag{19}$$

The actual measurement noise covariances are

$$\begin{aligned} \boldsymbol{R}_1 &= \text{diag}\left(\left[\boldsymbol{R}_p, \boldsymbol{R}_o, \boldsymbol{R}_{F_S}, \boldsymbol{R}_{M_S}\right]\right) \\ \boldsymbol{R}_2 &= \text{diag}\left(\left[\boldsymbol{R}_p, \boldsymbol{R}_o, \boldsymbol{R}_{F_S}, \boldsymbol{R}_{M_S}, \boldsymbol{R}_a, \boldsymbol{R}_\alpha, \boldsymbol{R}_\omega, \right]\right) \end{aligned} \tag{20}$$

with $\boldsymbol{R}_p = 10^{-6}$ m^2, $\boldsymbol{R}_o = 10^{-6}$, $\boldsymbol{R}_{F_S} = 10^{-3}$ N^2, $\boldsymbol{R}_{M_S} = 10^{-3}$ N^{2}m^2, $\boldsymbol{R}_a = 10^{-2}$ m^2/s^4, $\boldsymbol{R}_\alpha = 10^{-2}$ rad^2/s^4, and $\boldsymbol{R}_\omega = 10^{-3}$ rad^2/s^2. In the simulation, it is assumed that process and measurement covariances are constant. Then, the performance of the filter can be optimized by taking sensor measurements and determining the values of $\boldsymbol{R}_i$ offline. In reality, however, it is likely that the measurement noise varies over time. To take that effect into account, three different cases are considered in the filter evaluation:

$$\begin{aligned} &\text{(A)}\ \bar{\boldsymbol{R}}_i = \boldsymbol{R}_i \\ &\text{(B)}\ \bar{\boldsymbol{R}}_i = 10^2\boldsymbol{R}_i \\ &\text{(C)}\ \bar{\boldsymbol{R}}_i = 10^{-2}\boldsymbol{R}_i \end{aligned} \tag{21}$$

with $i \in \{1, 2\}$. While case A reflects a perfect knowledge of the actual measurement noise level, the cases B and C simulate an over- and an underestimation of the actual measurement noise level. Hence, the filter performance in the latter two cases is a measure for the robustness of the filter towards changing operating conditions.

In the simulation scenario I, the tool executes a sinusoidal motion in x-direction combined with a rotation of $-\pi$ around the x-axis, see Figure 3. The shown quaternions are

$$\boldsymbol{o}_1 = \cos\left(\frac{\varphi_x}{2}\right), \quad \boldsymbol{o}_2 = \sin\left(\frac{\varphi_x}{2}\right), \quad \boldsymbol{o}_3 = \boldsymbol{o}_4 = 0 \tag{22}$$

with the rotation angle $\varphi_x \in [-\pi, 0]$. The measured translational and rotational tool accelerations are depicted in Figure 4. During this motion, the following contact forces and torques occur:

$$\begin{aligned} \boldsymbol{F}_E &= \begin{cases} [20\text{ N},\ 0\text{ N},\ 0\text{ N}]^{\mathrm{T}}, & \text{if } 1\text{ s} < t < 4\text{ s} \\ [0\text{ N},\ 0\text{ N},\ 0\text{ N}]^{\mathrm{T}}, & \text{otherwise,} \end{cases} \\ \boldsymbol{M}_E &= \begin{cases} [0\text{ Nm},\ 0\text{ Nm},\ 5\text{ Nm}]^{\mathrm{T}}, & \text{if } 2\text{ s} < t < 3\text{ s} \\ [0\text{ Nm},\ 0\text{ Nm},\ 0\text{ Nm}]^{\mathrm{T}}, & \text{otherwise.} \end{cases} \end{aligned} \tag{23}$$

To evaluate the performance of the four filter designs (EKF with $\boldsymbol{y}_1$, EKF with $\boldsymbol{y}_2$, UKF with $\boldsymbol{y}_1$, UKF with $\boldsymbol{y}_2$), the force and torque estimation errors at time step k are defined as

$$\begin{aligned} \boldsymbol{e}_{F[k]} &= \boldsymbol{F}_{E[k]} - \hat{\boldsymbol{F}}_{E[k]} \\ \boldsymbol{e}_{M[k]} &= \boldsymbol{M}_{E[k]} - \hat{\boldsymbol{M}}_{E[k]}. \end{aligned} \tag{24}$$

For the evaluation, the performance of the filter with respect to both continuous and discrete changes of the environment forces and/or torques is of interest. Hence, the simulation is separated into different segments and each time step k is associated either with phase c (continuous) or phase d (discrete) according to

$$\begin{aligned} k_{c,[k]} &= \begin{cases} 1, & \text{if } t_{[k]} \in t_c \\ 0, & \text{otherwise} \end{cases} \\ k_{d,[k]} &= 1 - k_{c,[k]}. \end{aligned} \tag{25}$$

Discrete changes of the environment forces and torques occur at $t = 1$ s, $t = 2$ s, $t = 3$ s, and $t = 4$ s, cf. Equation (23). Hence, the continuous phase is defined as

$$t_c = \{[0, 1) \vee [1.5, 2) \vee [2.5, 3) \vee [3.5, 4) \vee [4.5, 5]\}. \tag{26}$$

With (24)–(26), the scalar error measures

$$\begin{aligned} e_{F,c} &= \sum_{k=1}^{N} Tk_{c,[k]} \left|\left|\boldsymbol{e}_{F[k]}\right|\right| \qquad e_{F,d} = \sum_{k=1}^{N} Tk_{d,[k]} \left|\left|\boldsymbol{e}_{F[k]}\right|\right| \\ e_{M,c} &= \sum_{k=1}^{N} Tk_{c,[k]} \left|\left|\boldsymbol{e}_{M[k]}\right|\right| \qquad e_{M,d} = \sum_{k=1}^{N} Tk_{d,[k]} \left|\left|\boldsymbol{e}_{M[k]}\right|\right| \end{aligned} \tag{27}$$

are defined, where $||\cdot||$ represents the Euclidean norm. In addition, the error measures

$$e_{F,\Sigma} = e_{F,c} + e_{F,d} \quad \text{and} \quad e_{M,\Sigma} = e_{M,c} + e_{M,d} \tag{28}$$

are used to evaluate the combined performance in phases c and d for force and torque estimation.

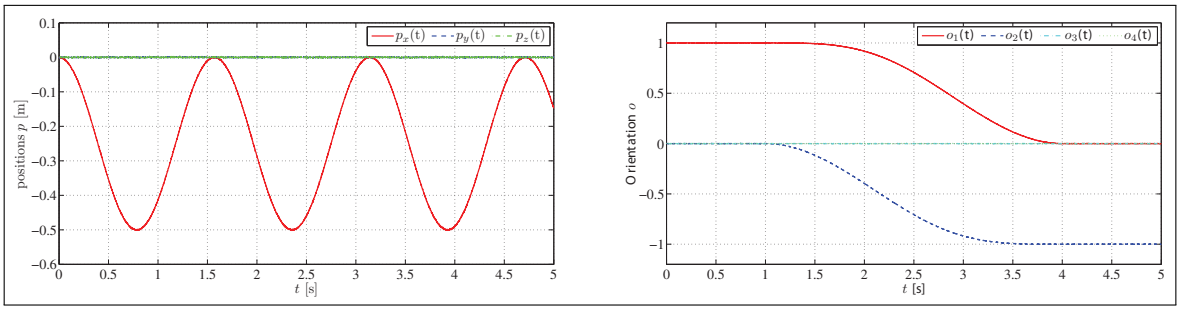

Fig. 3. Scenario I: Measured tool position (left) and orientation (right).

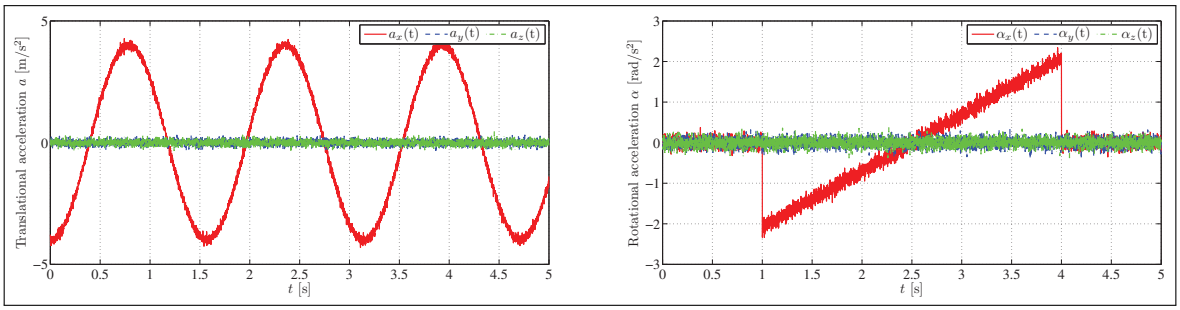

Fig. 4. Scenario I: Measured translational (left) and rotational tool acceleration (right).

4.2. Results

For case A, the measured sensor force, the true environment force, and the estimated environment force (UKF with $\boldsymbol{y}_2$) in the x-direction are depicted in Figure 5(a). The force estimation errors for the four different filter designs are illustrated in Figure 5(c). The forces along y- and z-axes are not displayed since no environment forces were applied in this direction. But they are, of course, considered in the calculation of the error measures. The measured sensor torques, the true environment torques, and the estimated environment torques (UKF with $\boldsymbol{y}_2$) around the three axes are depicted in Figure 5(d), (g), and (h). The corresponding estimation errors for the four filters are shown in Figure 5(b), (e), and (f). It should be noted that all three measured torques show significant deviations from zero, despite the fact that an environment torque is only applied around the z-axis (from $t = 2$ s to $t = 3$ s). These torques are created by two sources: the environment force $F_{E,x}$ and the inertial force $F_{I,x}$ due to the translational acceleration along the x-axis. The latter force also leads to measured torques since the tools center of mass and the force sensor coordinate system do not coincide.

4.3. Discussion

The quantitative results of the simulation for the cases A to C are summarized in Table 1 using the six error measures stated in (27) and (28). As will be detailed in the following, these results provide interesting information on the performance on the different filter designs. The first line of the table shows the values of the error measures when the measured forces $\boldsymbol{F}_S$ and torques $\boldsymbol{M}_S$ are assumed to be identical with the environment forces and torques. This can be considered as the worst-case scenario. As $\boldsymbol{F}_S$ and $\boldsymbol{M}_S$ are unfiltered data, the results are in this case independent of the assumed measurement noise. Hence, the error measures are identical for the cases A to C.

In case A, when using an observer design based on $\boldsymbol{y}_1$ (pose and F/T measurements), the combined error measures $e_{F,\Sigma}$ ($e_{M,\Sigma}$) can be reduced by approximately 82% (90%) compared with the worst-case scenario. Here, EKF and UKF design are performing almost equally well. By adding an acceleration sensor and using measurements $\boldsymbol{y}_2$ fused from the three sensor types, the performance can be further improved: the combined error measure $e_{F,\Sigma}$ is reduced by 63.9% for the EKF and by 65.2% for the UKF (compared with the filter with $\boldsymbol{y}_1$). It should be noted that the additional acceleration measurements mainly improve the error measure $e_{F,d}$ which evaluates discrete changes, whereas the improvements of $e_{F,c}$ are of minor influence. The same holds for the combined error measure $e_{M,\Sigma}$ when a filter design with $\boldsymbol{y}_2$ instead of $\boldsymbol{y}_1$ is used: the measure is reduced by 71.4% for the EKF and by 72.8% for the UKF. Again, the improvements are mainly associated with $e_{M,d}$. This is not surprising since the acceleration measurements are especially beneficial when sudden changes in the measurements occur.

In case B, the performance of all four filter designs degrades compared with case A. This is not surprising since the actual measurement noise is overestimated by a factor of 10^2. However, all filters still show a significant improvement compared to the raw measurements: the error measure $e_{F,\Sigma}$ is improved between 60.0% (EKF with $\boldsymbol{y}_1$) and 65.9%

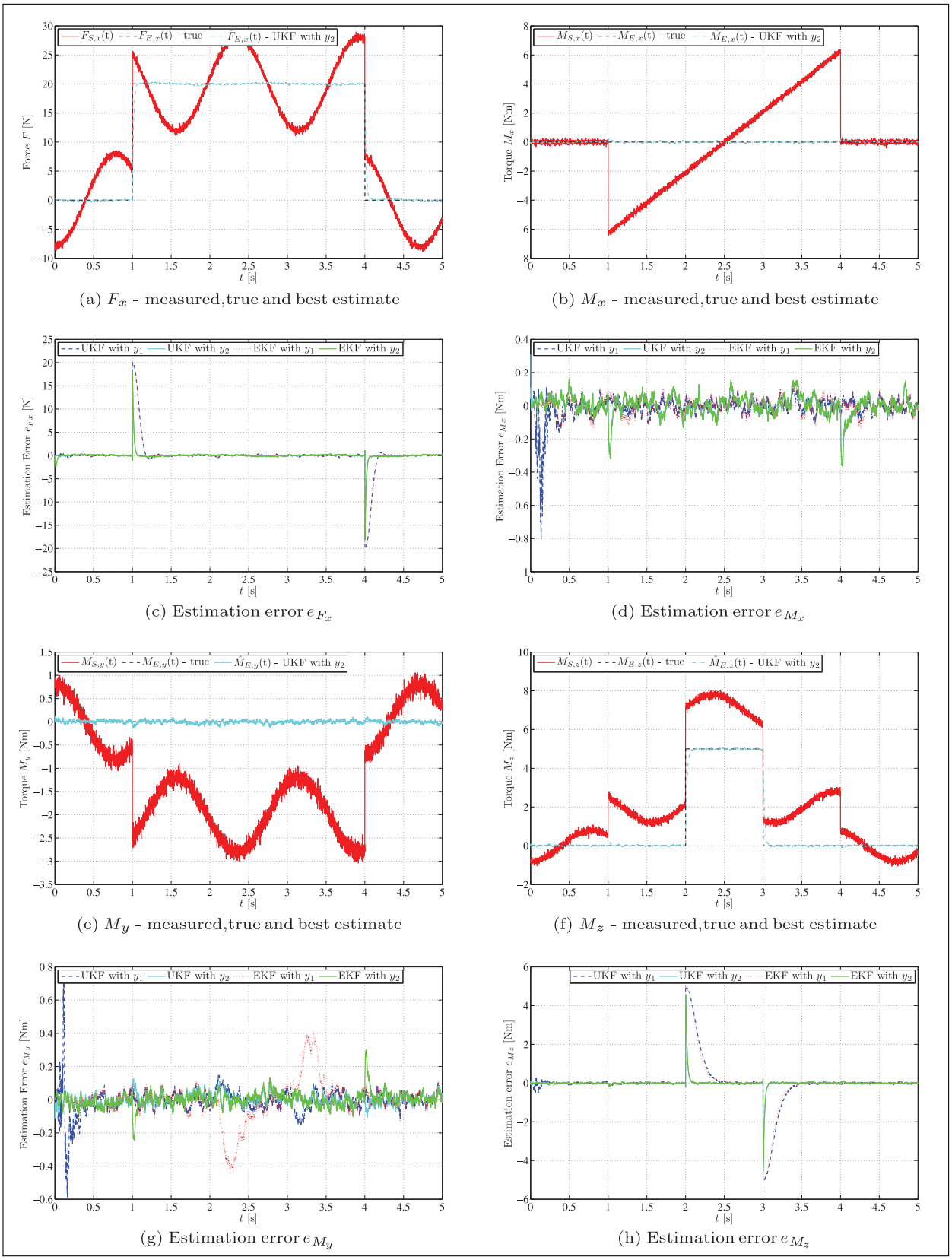

Fig. 5. Scenario I, Case A. (a) Measured force $F_{S,x}$, true environment force $F_{E,x}$ and best estimate of the environment force $\hat{F}_{E,x}$. (c) Estimation error e_{F_z} for the two UKF designs. The figure pairs (b) and (d), (e) and (g), and (f) and (h) show the corresponding results for the torques around the x-, y-, and z-axes.

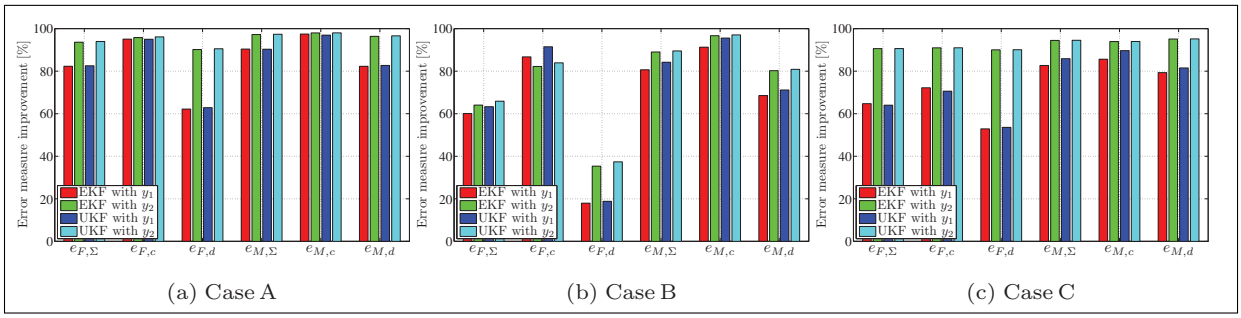

(a) Case A (b) Case B (c) Case C

Fig. 6. Error measures: improvements of the four filter designs compared with the measurements $\boldsymbol{F}_S$, $\boldsymbol{M}_S$.

Table 1. Scenario I: Error measures $e_{M,\Sigma}$, $e_{F,c}$, $e_{F,d}$, $e_{M,\Sigma}$, $e_{M,c}$, and $e_{M,d}$ for the different filter designs and cases A–C. In each column, the filters with the best performance are highlighted.

	Case A						Case B						Case C					
	$e_{F,\Sigma}$	$e_{F,c}$	$e_{F,d}$	$e_{M,\Sigma}$	$e_{M,c}$	$e_{M,d}$	$e_{F,\Sigma}$	$e_{F,c}$	$e_{F,d}$	$e_{M,\Sigma}$	$e_{M,c}$	$e_{M,d}$	$e_{F,\Sigma}$	$e_{F,c}$	$e_{F,d}$	$e_{M,\Sigma}$	$e_{M,c}$	$e_{M,d}$
meas. $\boldsymbol{F}_S, \boldsymbol{M}_S$	28.37	17.37	11.00	23.57	12.60	10.97	28.37	17.37	11.00	23.57	12.60	10.97	28.37	17.37	11.00	23.57	12.60	10.97
EKF with $\boldsymbol{y}_1$	5.02	0.86	4.16	2.27	0.32	1.94	11.33	2.31	9.03	4.55	1.10	3.46	10.01	4.83	5.18	4.08	1.81	2.27
UKF with $\boldsymbol{y}_1$	4.95	0.87	4.08	2.28	0.38	1.90	10.41	1.48	8.93	3.72	0.56	3.17	10.22	5.11	5.11	3.33	1.30	2.03
EKF with $\boldsymbol{y}_2$	1.81	0.73	1.08	0.65	0.25	0.40	10.20	3.09	7.11	2.59	0.42	2.17	2.67	1.57	1.10	1.30	0.77	0.54
UKF with $\boldsymbol{y}_2$	1.72	0.68	1.04	0.62	0.25	0.37	9.68	2.79	6.89	2.47	0.37	2.10	2.66	1.56	1.09	1.29	0.76	0.53

(UKF with $\boldsymbol{y}_2$), the error measure $e_{M,\Sigma}$ between 80.7% (EKF with $\boldsymbol{y}_1$) and 89.5% (UKF with $\boldsymbol{y}_2$). Remarkably, in case B, the error measure $e_{F,c}$ of the observer designs with $\boldsymbol{y}_1$ is smaller than that of their counterparts with $\boldsymbol{y}_2$. However, considering the combined measure $e_{F,\Sigma}$, the designs with $\boldsymbol{y}_2$ are still superior.

In case C, the underestimation of the measurement noise by a factor of 10^{-2} results for all four filters in a performance which is between their respective performance in cases A and B. However, the results of the filter designs with $\boldsymbol{y}_1$ are only slightly better than in case B: for the EKF (UKF), the measure $e_{F,\Sigma}$ is improved by 11.7% (1.8%) and the measure $e_{M,\Sigma}$ by 10.3% (10.5%). In contrast, the results of the filter designs with $\boldsymbol{y}_1$ are significantly better in case C than in case B: for the EKF (UKF), the measure $e_{F,\Sigma}$ is improved by 73.8% (72.5%) and the measure $e_{M,\Sigma}$ by 49.8% (47.8%). Also, for the filter designs with $\boldsymbol{y}_2$, it is interesting to see that the decline in performance compared with case A is mainly caused by a worse performance in the continuous phases (error measures $e_{F,c}$ and $e_{M,c}$). The error measures $e_{F,d}$ and $e_{M,d}$ for discrete changes, however, are hardly affected by the underestimation of the measurement noise. This result corresponds with the intuitive idea of the functional principles of the filters.

Overall, the UKF-based design with $\boldsymbol{y}_2$ showed the best performance although in most cases, there is only a small improvement when compared to the EKF with $\boldsymbol{y}_2$. As an additional advantage of the design with the UKF, the calculation of the partial derivatives of process and measurement equation is not necessary, compare (15). While there is a significant performance difference between the designs with $\boldsymbol{y}_2$ and $\boldsymbol{y}_1$, the observers based on the latter measurement vector still show a fundamental improvement compared to the raw measurements. For the designs with $\boldsymbol{y}_1$, the performance of EKF and UKF is comparable with each of them giving better results in some cases.

5. Experiment

In order to verify the simulation, the filter designs were also evaluated using real experimental data. In the following, this will be denoted as scenario II. As in simulation scenario I, the main focus is on the compensation of inertial effects and the rejection of measurement noise. While gravitational forces and torques occurred during the experiments, their effects have been eliminated from the measured forces and torques that are shown in the results and the discussion.

5.1. Scenario

The experimental setup and the parameters of the experiment are depicted in Figure 8: an extension spring with spring constant $c = 0.303$ N/mm is attached to the end effector in order to generate a known environment force when the robot is moving. The dynamic parameters of the end effector were determined based on its CAD model. The forces, torques, and accelerations are measured with a 12-DOF sensor from JR3, see Figure 8. The sensor outputs force, torque, and acceleration data at 8 kHz, where linear accelerations can be measured up to $5g$ with a resolution of $0.01g$ and angular accelerations can be measured up to 100 rad/s^2 with a resolution of 0.1 rad/s^2. The measurement noise covariances $\boldsymbol{R}_i$ were determined with the robot control running and the robot commanded to remain in a stationary pose. The following values were obtained:

$$\begin{aligned} \boldsymbol{R}_1 &= \operatorname{diag}\left(\left[\boldsymbol{R}_p, \boldsymbol{R}_o, \boldsymbol{R}_{F_S}, \boldsymbol{R}_{M_S}\right]\right) \\ \boldsymbol{R}_2 &= \operatorname{diag}\left(\left[\boldsymbol{R}_p, \boldsymbol{R}_o, \boldsymbol{R}_{F_S}, \boldsymbol{R}_{M_S}, \boldsymbol{R}_a, \boldsymbol{R}_\alpha, \boldsymbol{R}_\omega, \right]\right) \end{aligned} \tag{29}$$

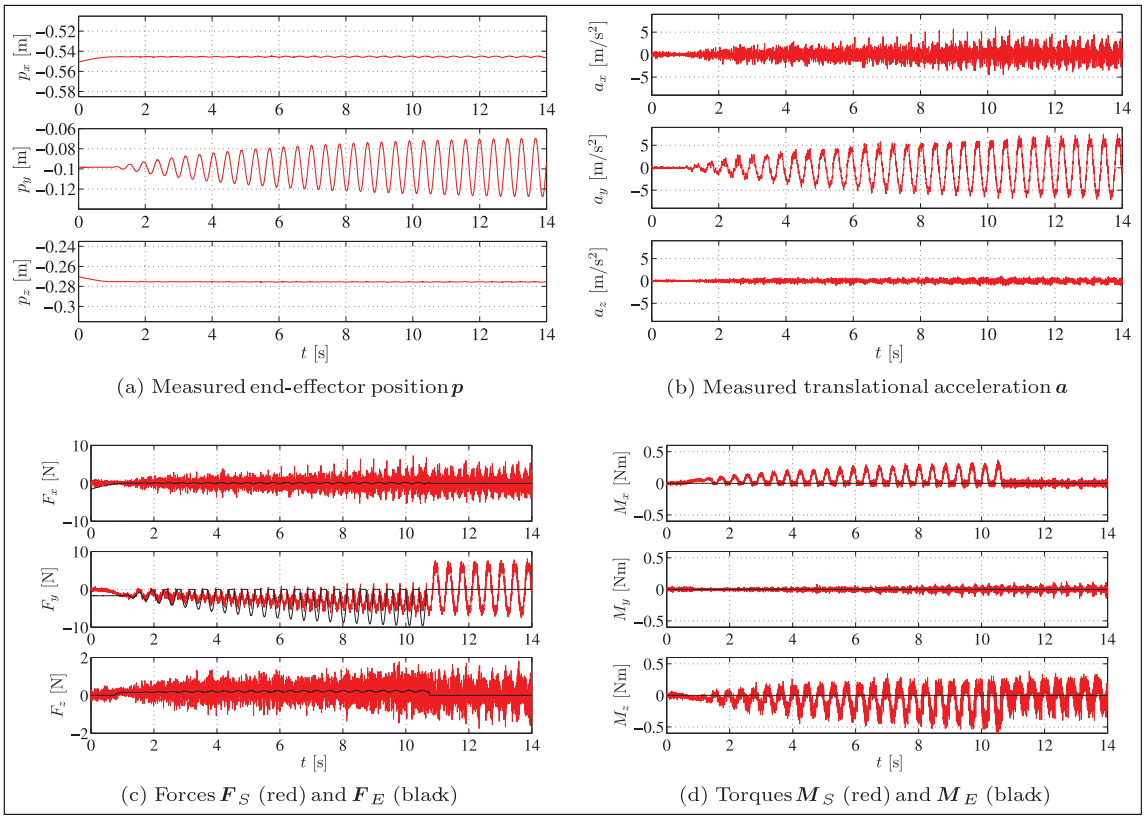

Fig. 7. Scenario II: (a) measured position $\boldsymbol{p}$ and (b) measured translational acceleration $\boldsymbol{a}$ of the end effector. (c) The measured forces $\boldsymbol{F}_S$/torques $\boldsymbol{M}_S$ and (d) the true environment forces $\boldsymbol{F}_E$/torques $\boldsymbol{M}_E$.

with $\boldsymbol{R}_p = 10^{-6}$ m^2, $\boldsymbol{R}_o = 10^{-6}$, $\boldsymbol{R}_{F_S} = 3 \times 10^{-3}$ N^2, $\boldsymbol{R}_{M_S} = 10^{-3}$ N^{2}m^2, $\boldsymbol{R}_a = 10^{-3}$ m^2/s^4, $\boldsymbol{R}_\alpha = 1$ rad^2/s^4, and $\boldsymbol{R}_\omega = 10^{-3}$ rad^2/s^2. The process noise covariance $\boldsymbol{Q}$ is set to the same values as in the simulation.

From time $t = 0$ to 1 s, the end effector moves to a specified position $\boldsymbol{p}_0$ to attach the spring. Starting at $t_1 = 1$ s, the end effector executes a sinusoidal motion in y-direction

$$p_y(t) = p_{0,y} + 0.03\left(1 - \mathrm{e}^{-0.2(t-t_1)}\right)\sin\left(15(t-t_1)\right), \quad (30)$$

while $p_x(t)$ and $p_z(t)$ remain constant. After 23 cycles ($t = 10.7$ s), the spring is detached from the end effector while the sinusoidal motion is continued until the end of the experiment at $t = 14$ s.

The measured end effector position and acceleration are depicted in Figure 7(a) and (b). The forces $\boldsymbol{F}_S$ measured with the F/T sensor and the true environment forces $\boldsymbol{F}_E$ are illustrated in Figure 7(c). The true environment forces caused by the spring are calculated based on the actual end effector position during the task execution. As the spring is aligned with the y-axis, a perfect trajectory execution would cause only forces in y-direction. However, the error between desired and actual position also results in small forces in z-direction. Owing to inertial effects and noise, the measured sensor forces deviate strongly from the actual forces exchanged with the environment, cf. Figure 7(c).

Similarly, Figure 7(d) shows the measured torques $\boldsymbol{M}_S$ and the true environment torques $\boldsymbol{M}_E$. As interaction with the environment occurs only via the extension spring, the true environment torques are zero. Again, there are significant deviations between the measured and the true environment torques. In addition to inertial effects and measurement noise, these deviations are also caused by the spring: the off-center contact point creates torques around the x- and z-axes.

For the evaluation, the force and torque estimation errors as defined in (24) are used. In contrast to the simulation, there is no differentiation between continuous and discrete phases. Hence, only the combined error measures $e_{F,\Sigma}$ and $e_{M,\Sigma}$ are utilized for the evaluation of the performance, cf. (28).

5.2. Results

The measured sensor force, the true environment force, and the estimated environment force (UKF with $\boldsymbol{y}_2$) in the y-direction are depicted in Figure 10(a). The force estimation errors for the four different filter designs are illustrated in Figure 10(b). For the two observers based on measurement vector $\boldsymbol{y}_1$, the estimation error shows very similar behavior: during contact with the environment, the estimates lag behind the actual forces leading to errors of up to 7 N. The

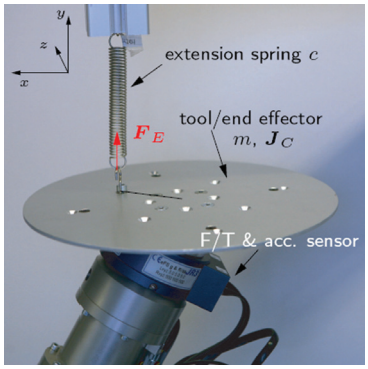

Parameters	Units
$m = 0.98$	[kg]
$\boldsymbol{J}_C^C = 10^{-3} \begin{bmatrix} 1.83 & 0.161 & 0.414 \\ 0.161 & 1.87 & -0.436 \\ 0.414 & -0.436 & 2.82 \end{bmatrix}$	[kg·m^2]
$\boldsymbol{r}_{CS}^C = [0.0001, 0.00001, -0.0446]^{\mathrm{T}}$	[m]
$\boldsymbol{r}_{CE}^C = [0.0549, -0.015, 0.0096]^{\mathrm{T}}$	[m]
$T_s = 0.001$	[s]
$c = 0.303$	[N/mm]

Fig. 8. Scenario II: Experimental setup with a spring attached to one end effector of the dual-arm robot and dynamic parameters of the tool, relative positions of the F/T sensor and the contact point of the environment interaction, and the sampling time.

	$e_{F,\Sigma}$	$e_{M,\Sigma}$
Measure $\boldsymbol{F}_S$,$\boldsymbol{M}_S$	55.38	2.95
EKF with $\boldsymbol{y}_1$	23.70	0.59
UKF with $\boldsymbol{y}_1$	23.60	0.53
EKF with $\boldsymbol{y}_2$	5.99	0.23
UKF with $\boldsymbol{y}_2$	5.99	0.21

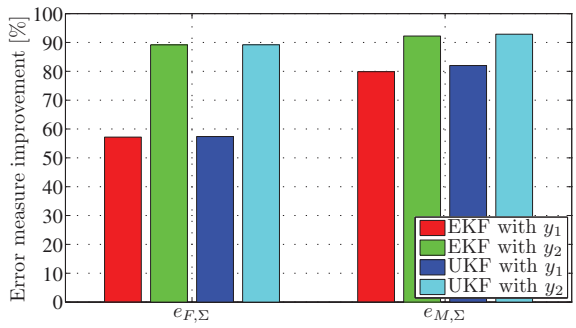

Fig. 9. Scenario II. Error measures: improvements of the four filter designs compared with the measurements $\boldsymbol{F}_S$, $\boldsymbol{M}_S$. In each column, the filters with the best performance are highlighted.

estimation errors of the $\boldsymbol{y}_2$-based designs are also almost identical. However, the maximum estimation error for these designs is only 1.8 N. From Figure 10(a), it is evident that measured sensor forces cannot be directly used in a force control scheme: in both phases, there is a significant deviation between the measurements and the actual environment forces. During the contact phase (from 1 to 10.8 s), the environment/spring force $\boldsymbol{F}_E$ partially compensates the inertial forces $\boldsymbol{F}_I$. During the free space motion (10.8 to 14 s), the measured forces reflect the inertial forces caused by the sinusoidal motion with increasing amplitude.

The measured sensor torques, the true environment torques, and the estimated environment torques (UKF with $\boldsymbol{y}_2$) around the x- and z-axes are depicted in Figure 11(a) and (c). The corresponding estimation errors for the four filters are shown in Figure 11(a) and (d). As for the forces, the estimation errors for UKF and EKF with the same measurement vector are very similar. Furthermore, the maximum errors of the $\boldsymbol{y}_2$-based designs (0.04 Nm) are considerably lower than those of the filters with $\boldsymbol{y}_1$ (0.1 Nm). In analogy to the forces, the deviations between measured torques $\boldsymbol{M}_S$ and actual environment torques $\boldsymbol{M}_E$ depicted in Figure 11(a) and (c) illustrate the importance of the observer for a reliable force control performance.

5.3. Discussion

The quantitative results are summarized in Figure 9 using the two error measures $e_{F,\Sigma}$ and $e_{M,\Sigma}$. Again, the first row of the table shows the values of the error measures when the measured forces $\boldsymbol{F}_S$ and torques $\boldsymbol{M}_S$ are assumed to be identical with the environment forces and torques. This can be considered as the worst-case scenario.

When using an observer design based on $\boldsymbol{y}_1$ (pose and F/T measurements), the combined cumulative error measures $e_{F,\Sigma}$ ($e_{M,\Sigma}$) can be reduced by approximately 57% (80%) compared with the worst-case scenario. Here, EKF and UKF design are performing almost equally well. By adding an acceleration sensor and using measurements $\boldsymbol{y}_2$ fused from the three sensor types, the performance can be further improved: the combined error measure $e_{F,\Sigma}$ is reduced by 74.7 % for the EKF and by 74.6 % for the UKF (compared with the filter with $\boldsymbol{y}_1$). The same holds for the combined error measure $e_{M,\Sigma}$ when a filter design with $\boldsymbol{y}_2$ instead of $\boldsymbol{y}_1$ is used: the measure is reduced by 61.3% for the EKF and by 60.5% for the UKF.

Overall, the experimental results are in accordance with those of the simulation: first, EKF- and UKF-based observer designs perform almost equally well; second, the

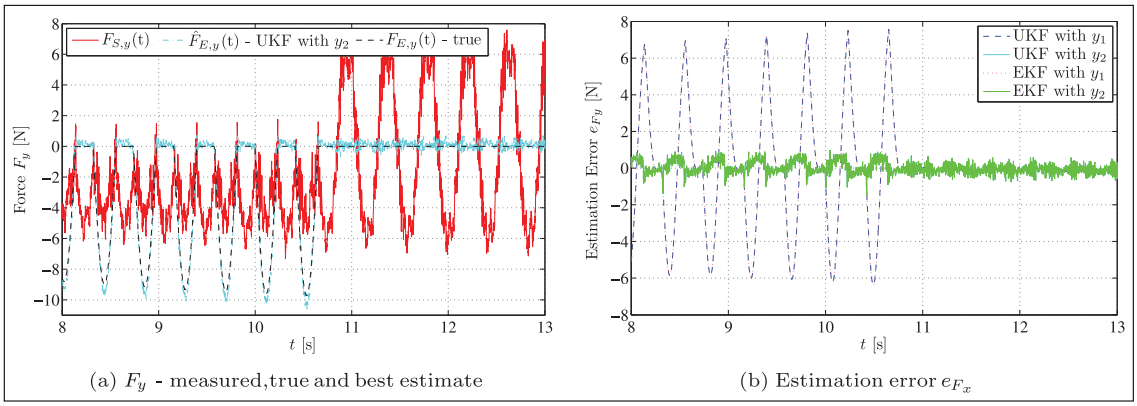

(a) F_y - measured,true and best estimate (b) Estimation error e_{F_x}

Fig. 10. Scenario II: (a) measured force $F_{S,y}$, true environment force $F_{E,y}$ and best estimate of the environment force $\hat{F}_{E,y}$; (b) estimation error e_{F_y} for the two UKF and the two EKF designs.

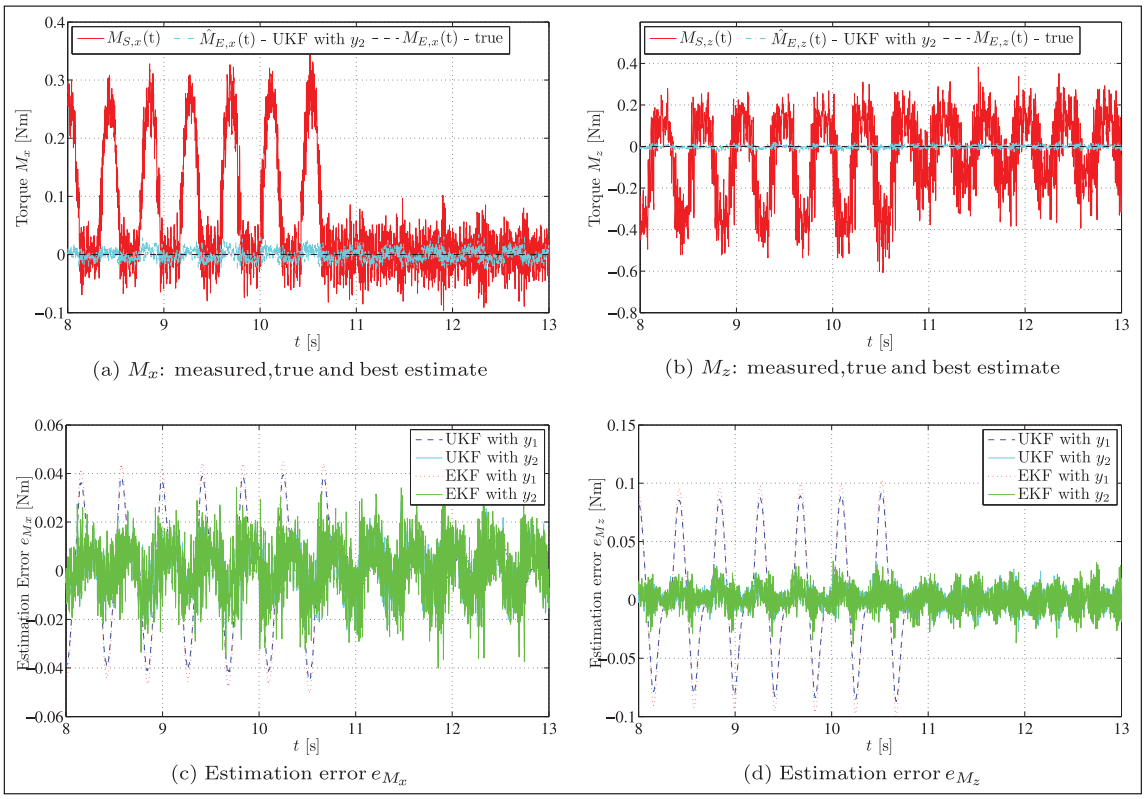

(a) M_x: measured,true and best estimate (b) M_z: measured,true and best estimate

(c) Estimation error e_{M_x} (d) Estimation error e_{M_z}

Fig. 11. Scenario II: (a) measured torque $M_{S,x}$, true environment torque $M_{E,x}$ and best estimate of the environment torque $\hat{M}_{E,x}$; (c) estimation error e_{M_x} for the two UKF and the two EKF designs; (b),(d) the corresponding results for the torque around the z-axis.

designs with the extended measurement vector $\boldsymbol{y}_2$ show a significant performance improvement compared with designs based on $\boldsymbol{y}_1$. The observers with $\boldsymbol{y}_1$, in turn, still show significant improvements compared to the measured values.

6. Conclusion

This paper presented a sensor fusion approach to improve the performance of interaction control schemes by estimating the actual environmental forces and torques. The continuous- and discrete-time system model was derived using quaternion notation for the description of the tool orientation. Based on the system model, the design of six-DOF F/T observers was discussed. Here, designs based on the EKF and on the UKF were presented. For both designs, two different measurement vectors have been considered: the first one uses pose and F/T measurements while the second one also uses acceleration and (rotational) velocity measurements.

The four filter designs were first evaluated in a six-DOF simulation scenario. Particular interest was paid to the

robustness of the filter designs towards changing environment conditions. To this end, the simulation was performed in three different conditions: a perfectly known, an overestimated, and an underestimated measurement noise. Six error measures were introduced to evaluate the performance for force and torque estimation during continuous and discrete phases. Despite the decline in performance, the variation of the measurement noise showed that the filters can significantly improve the contact F/T estimation even for inaccurate estimates of the measurement noise levels. For the observer designs with extended measurement vector, the underestimation of the measurement noise was less critical than the overestimation. For the designs with pose and F/T measurements, the effects of over- and underestimation were comparable.

In addition to the simulation, a six-DOF experiment was conducted to verify the results. For both, simulation and experiment, the UKF with the extended measurement vector performed best. Although it showed in most of cases only small improvements compared with the EKF with extended measurements, it offers the additional benefit that the calculation of process and measurement Jacobians is not needed which makes the UKF easier to implement.

Acknowledgments

The first author gratefully thanks the German National Academic Foundation for their support.

Funding

This research received no specific grant from any funding agency in the public, commercial, or not-for-profit sectors.

References

Garcia J, Robertsson A, Ortega J and Johansson R (2008) Sensor fusion for compliant robot motion control. *IEEE Transactions on Robotics* 24: 430–441.

Garcia JG, Robertsson A, Ortega JG and Johansson R (2004) Sensor fusion of force and acceleration for robot force control. In: *Proceedings of 2004 IEEE/RSJ International Conference on Intelligent Robots and Systems*, Sendai, Japan, pp. 3009–3014.

Garcia JG, Robertsson A, Ortega JG and Johansson R (2005a) Automatic calibration procedure for a robotic manipulator force observer. In: *Proceedings of the 2005 IEEE International Conference on Robotics and Automation*, Barcelona, Spain, pp. 2703–2708.

Garcia JG, Robertsson A, Ortega JG and Johansson R (2005b) Force and acceleration sensor fusion for compliant robot motion control. In: *Proceedings of the 2005 IEEE International Conference on Robotics and Automation*, Barcelona, Spain, pp. 2709–2714.

Garcia JG, Robertsson A, Ortega JG and Johansson R (2006) Generalized contact force estimator for a robot manipulator. In: *Proceedings of the 2006 IEEE International Conference on Robotics and Automation*. Orlando, Florida, pp. 4019–4024.

Julier SJ and Uhlmann JK (1997) *A New Extension of the Kalman Filter to Nonlinear Systems*. Technical report, The Robotics Research Group, Department of Engineering Science, The University of Oxford.

Julier SJ and Uhlmann JK (2004) Unscented filtering and nonlinear estimation. *Proceedings of the IEEE* 92: 401–422.

Julier SJ, Uhlmann JK and Durrant-Whyte HF (1995) A new approach for filtering nonlinear systems. In: *Proceedings of the American Control Conference*, volume 3, Seattle, WA, pp. 1628–1632.

Khatib O (1987) A unified approach for motion and force control of robot manipulators: the operational space formulation. *IEEE Journal on Robotics and Automation* 3(1): 43–53. DOI: 10.1109/JRA.1987.1087068.

Koch H, Konig A, Weigl-Seitz A, Kleinmann K and Suchy J (2011) Force, acceleration and vision sensor fusion for contour following tasks with an industrial robot. In: *Proceedings IEEE International Symposium on Robotic and Sensors Environments (ROSE)*, Montreal, Canada, pp. 1 –6. DOI: 10.1109/ROSE.2011.6058516.

Kraft E (2003) A quaternion-based Unscented Kalman Filter for orientation tracking. In: *Proceedings of the Sixth International Information Fusion Conference*, vol. 1, Cairns, Queensland, Australia, pp. 47–54.

Kröger T, Kubus D and Wahl F (2006) 6D force and acceleration sensor fusion for compliant manipulation control. In: *Proceedings IEEE/RSJ International Conference on Intelligent Robots and Systems*, Beijing, China, pp. 2626–2631.

Kubus D, Kröger T and Wahl F (2008) Improving force control performance by computational elimination of non-contact forces/torques. In: *Proceedings IEEE International Conference on Robotics and Automation (ICRA 2008)*, Pasadena, CA, pp. 2617–2622.

Lefebvre T (2005) *Nonlinear Kalman Filtering for Force-Controlled Robot Tasks*. Berlin: Springer-Verlag.

Lin ST (1997) Force sensing using Kalman filtering techniques for robot compliant motion control. *Journal of Intelligent and Robotic Systems* 18: 1–16.

Mason M and Lynch K (1993) Dynamic manipulation. In: *Proceedings IEEE/RSJ International Conference on Intelligent Robots and Systems 1993 (IROS'93)*, vol. 1, pp. 152–159. DOI: 10.1109/IROS.1993.583093.

Natale C (2003) *Interaction Control of Robot Manipulators - Six-Degrees-of-Freedom Tasks*. New York: Springer.

Siciliano B, Sciavicco L, Villani L and Oriolo G (2008) *Robotics - Modelling, Planning and Control*. New York: Springer.

Uchiyama M and Kitagaki K (1989) Dynamic force sensing for high-speed robot manipulation using Kalman filtering techniques. In: *Proceedings 28th IEEE Conference on Decision and Control*, pp. 2147–2152.

Wan E and Van Der Merwe R (2000) The Unscented Kalman Filter for nonlinear estimation. In: *Proceedings IEEE Adaptive Systems for Signal Processing, Communications, and Control Symposium*, pp. 153–158.

Welch G and Bishop G (2006) *An Introduction to the Kalman Filter*. Technical report, Department of Computer Science, University of North Carolina at Chapel Hill.

Wittenburg J (2007) *Dynamics of Multibody Systems*. New York: Springer.